Near-edge x-ray absorption and emission of cyanates and thiocyanates

Karina Bzheumikhova, John Vinson, Rainer Unterumsberger, Yves Kayser, Terrence Jach, and Burkhard Beckhoff

Phys. Rev. B **106**, 125133 — Published 20 September 2022

DOI: 10.1103/PhysRevB.106.125133

Near edge X-ray absorption and emission of cyanates and thiocyanates

Karina Bzheumikhova,[1, *] John Vinson,[2] Rainer Unterumsberger,[1]
Yves Kayser,[1] Terrence Jach,[2] and Burkhard Beckhoff[1]
[1] *Physikalisch-Technische Bundesanstalt, Abbestraße 2-12, 10587 Berlin, Germany*
[2] *Material Measurement Laboratory, National Institute of Standards and Technology, Gaithersburg, MD 20899*
(Dated: August 2, 2022)

The comparability and reliability of the analysis of the electronic structure of selected cyanates and thiocyanates at the nitrogen K edge based on BSE calculations has been investigated in this work. Using high-resolution X-ray spectroscopy with calibrated instrumentation reliable and reproducible experimental results for X-ray absorption spectroscopy (XAS) and resonant inelastic X-ray scattering (RIXS) were achieved. These results were used to validate theoretical modeling with first-principle calculations based on the Bethe-Salpeter equation approach for the excited-state interactions. Furthermore, radiation induced damages occurring in the samples are correlated with absolute doses.

I. INTRODUCTION

In this study, we have used instrumentation, which has been carefully calibrated at selected excitation and emission photon energies, to provide experimental data to validate theoretical calculations with the OCEAN code [6, 13] based on a Bethe-Salpeter equation (BSE) approach [6]. The systematic study of model systems presented here allows for a detailed comparison between experimental and theoretical data by focusing on a single element, in this case the nitrogen atom, and using the same set of calculation parameters except for the crystal structure.

The electronic structure of a chemical compound depends on the atoms involved as well as their respective distances and coordination geometry. Recent publications on iron-sulfur compounds [15] and titanium oxides [16] have already shown the discrimination capabilities and validation potential of calculations when comparing experimental and theoretical findings around K edges of selected early transition metals. In addition, the prediction capabilities of the OCEAN code have been shown in the analysis of various nitrogen compounds [2, 17, 18]. Specifically, the electronic structure of ionic crystals with molecular sub-components, e.g. $LiNO_3$ [1] and NH_4NO_3 [2], has been investigated by comparing experimental near-edge x-ray absorption and emission spectroscopy results with first-principles calculations. This paper continues this exploration by examining ionic crystals whose anions have a linear spatial structure.

The linear structure of the compounds provides the opportunity to study nearest-neighbor and next-nearest-neighbor interactions in crystal structures and their influence on the electronic structure. Furthermore, these compounds are an interesting benchmark system for the capabilities of the used quantum code packages to correctly predict the electronic structure of ionically bonded constituents with the necessity to include long range interactions. The BSE approach is a first-principles method whose only truly free parameters, apart from certain choices of pseudopotentials, are the positions of the atoms in the structure being simulated. The excited-state interactions are included explicitly on top of the ground-state band structure. The mix of extended and ionic systems with small linear molecule constituents provides a good test case for these kinds of theoretical calculations.

We analyze cyanates CNO^- and thiocyanates SCN^- with different metal cations using high-resolution X-ray spectroscopic experiments to elucidate their electronic structure. Importantly, the investigation with synchrotron radiation requires the minimization of radiation damage [14]. Several methods for mitigating radiation damage are assessed in this work and a threshold values for dosage is determined.

The electronic structure of cyanates and thiocyanates has been studied in the past using both X-ray absorption and infrared spectroscopy [7, 8]. We use X-ray absorption spectroscopy (XAS) on cyanates and thiocyanates to analyse transitions involving the occupied states [9, 10]. In addition, resonant inelastic X-ray scattering (RIXS) allows for a simultaneous investigation of both states, occupied and unoccupied, therefore providing supplementary information on an energy-dependent development of specific spectroscopic features. For an in-depth understanding of the electronic landscape and a meaningful comparison with first principles calculations it is imperative to use moderate to high resolution techniques with energy resolving powers $E/\Delta E$ up to a few thousand.

II. EXPERIMENTAL SETUP AND MEASUREMENT PROCEDURE

A. Experimental method

The experiments were conducted at the plane-grating monochromator (PGM) beamline [19] for undulator radiation in the laboratory of the Physikalisch-Technische Bundesanstalt (PTB) at the electron storage ring BESSY

---

[*] karina.bzheumikhova@ptb.de

II. The beamline provides tunable linearly polarized undulator radiation in the soft X-ray range with photon energies between 78 eV and 1860 eV with high spectral purity and photon flux.

For X-ray absorption measurements the induced fluorescence radiation is detected with a silicon drift detector (SDD) with a known spectral response and efficiency [20, 21]. The absorption measurements were conducted near the N K edge. The near-edge X-ray absorption fine structure (NEXAFS) measurements were performed at an incident and takeoff angle of $\theta = 45°$ [22]. The incident photon flux is determined with a calibrated diode. The samples were inserted in an ultra-high vacuum environment allowing for the use of soft X-ray radiation.

The RIXS data have been recorded using a wavelength-dispersive spectrometer (WDS) [23–25]. The fluorescence radiation is analyzed by a spherical grating spectrometer and detected with a charge-coupled device (CCD) positioned on the Rowland circle. The optical source is defined by means of an entrance slit which is also positioned on the Rowland circle between the grating and the sample. The resolving power of the spectrometer was set to $E/\Delta E = 800$. Additionally, a vertical slit and a horizontal slit are placed between the entrance slit and the grating, acting as an aperture against stray light. The vertical slit collimates horizontally so that the detector is not illuminated outside of its active area in the non-dispersive direction while the horizontal slit restricts the illuminated area of the grating in the dispersive direction. This way the solid angle of acceptance of the WDS is defined. The compact design of the WDS ensures high-stability which allows for an absolute calibration of the instrument [24] with respect to both its detection efficiency and response function. The presented work uses the absolute calibration of the energy scale to ensure a good comparability of the results with literature – provided that the calibration concepts are comparable – and with theoretical calculations. The achieved spectral resolution was determined by recording the elastic scattering of the incident monochromatic undulator radiation from a boron nitride sample which was used to determine the response function of the spectrometer.

In order to ensure physically traceable, reliable, and comparable absolute values, both the incident as well as the emission energy scale were calibrated carefully. The excitation energy from the monochromator was calibrated from the absorption of well-known vibrational resonances of gas phase N_2 [26]. The emission energy scale of the WDS used for RIXS measurements was calibrated by elastic scattering from a boron nitride sample, thus transferring the monochromator's energy scale to the spectrometer.

Five different commercially available materials (Sigma-Aldrich) in powder form were analyzed: sodium cyanate (NaOCN), sodium thiocyanate (NaSCN), potassium cyanate (KOCN), potassium thiocyanate (KSCN), and copper thiocyanate (CuSCN). The copper cation, with its filled $3d$ valence orbitals, yields a significantly different electronic structure compared to the alkali metals sodium and potassium. However, copper cyanate is not stable and has not been included. The samples were prepared in two different ways. The first set of samples was pressed into pellets with 10 mm in diameter and approximately 2 mm in thickness. The other set of samples was pressed as a thin layer of grains into an indium foil. The pellets were used for the RIXS and XAS measurements whereas the samples pressed in indium foil were used to measure the sample current during XAS measurements to analyse surface effects which are not affected by self-absorption.

B. Radiation damage considerations

The measurement of light elemental compounds requires special care in order to minimize radiation damage [14, 27, 28]. During the XAS measurements the sample position was changed after each energy step. Each X-ray emission spectrum measured at a specific incident photon energy is recorded during a 20-minute measurement time. To reduce any possible influence of radiation damage, the sample positions were changed between each spectrum during the RIXS measurements as well. Nevertheless, to evaluate the effects of synchrotron radiation in the X-ray range on the cyanates and thiocyanates during this acquisition time in particular, repeated NEXAFS measurements on pellets and compounds pressed in indium foil were conducted.

Figures 1(a) and 1(b) show NEXAFS measurements under fluorescence detection ($\Delta E = 0.25$ eV) at the N K edge with increasing values of the radiation dose on a selected sample spot. Repeated NEXAFS measurements of the thiocyanate indicate a stable behaviour suggesting that the electronic structure of the sample was not changed with increasing radiation dose. However, measurements of the cyanates showed a significant change of the fine structure. The first measurement has one distinct peak at 400.5 eV incident energy, whereas the subsequent NEXAFS measurements indicate a splitting into two peaks. The peak at lower energies around 399 eV is growing with increasing radiation dose and the main peak is shifted to higher energies around 400.75 eV.

n order to better investigate and differentiate surface and bulk effects, NEXAFS measurements were also taken by means of the sample current, Figures 1(c) and 1(d). The sample current measures Auger and photoelectrons escaping from the sample surface and is not affected by self-absorption. Additionally, the mean free path of the electrons is in the few nm regime, making sample current measurements only sensitive to the near-surface region. However, additional surface phenomena like secondary ionization or plasmon loss effects may occur [29]. In addition, the surface chemistry may be different or contaminated in comparison to the bulk.

The comparison of the measurement of the fluorescence line intensity and the sample current confirms the stabil-

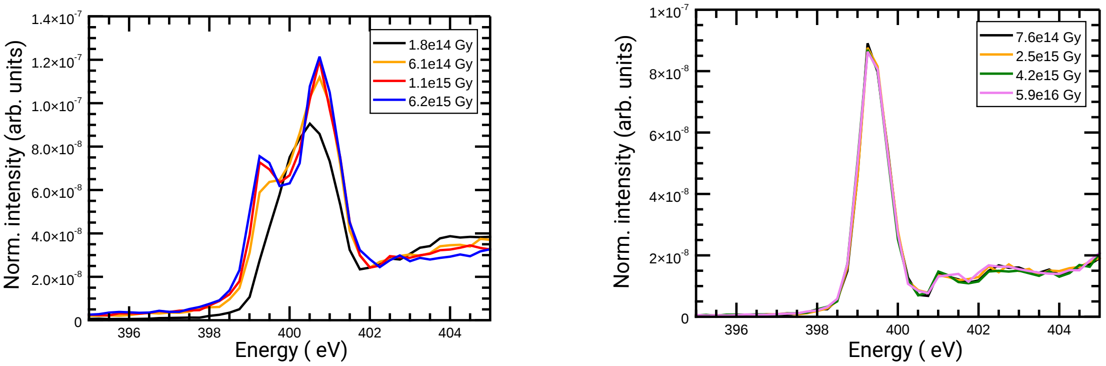

(a) NaOCN (b) NaSCN

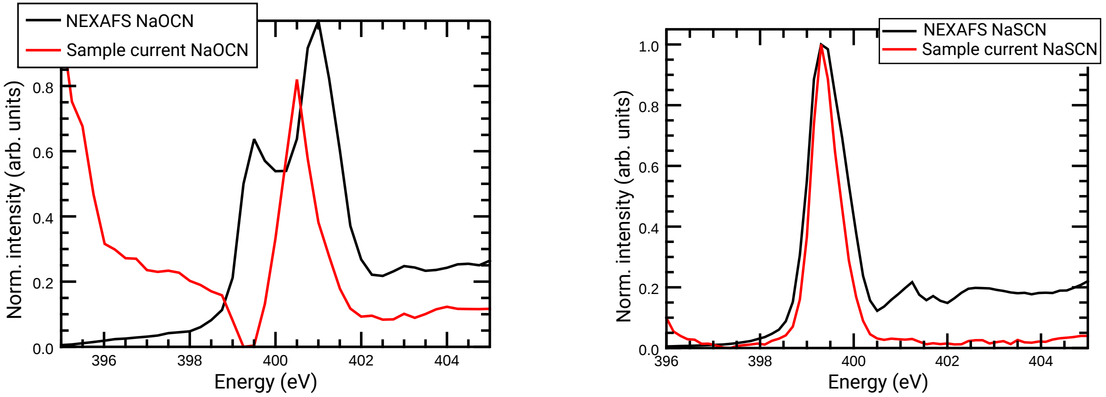

(c) NaOCN (d) NaSCN

FIG. 1. Repeated NEXAFS measurements under fluorescence detection of NaOCN (a) and NaSCN (b) at the N K edge with increasing radiation dose. Comparison of the fluorescence line intensity (black) and sample current (red) measurements of NaOCN (c) and NaSCN (d) at the nitrogen K edge. For the sake of clarity, spectra (c) and (d) have been normalized to the maximum intensity which has been set to 1.

ity of the thiocyanate [Fig. 1(d)]. In strong contrast, the cyanate sample current with a peak at 400.5 eV indicates that the radiation damage induced changes are not observed on the surface but rather in the bulk. Further analysis of the peak at 400.75 eV show that the C-N bond is being broken, and N_2 gas was trapped in the bulk. This was confirmed through high-energy-resolved measurements of the peak compared to the N_2 gas measurements during the calibration of the energy scale of the beamline. Further information can be found in the Supplemental Material [35].

We conclude that due to the extended measurement time required for the acquisition of a RIXS map, radiation damage free RIXS of the cyanates is not possible. For the cyanates only XAS results are presented in Section IV.

Our results allow us to quantify the X-ray induced radiation damage to cyanates. For NaOCN, a radiation dose above approximately $1.8 \cdot 10^{14}$ Gy leads to radiation damage, a potential problem in general when studying light element chemical compounds. Using this information, future measurements can be adjusted by constantly moving the sample during the exposure time, reducing the incident dose per area accordingly, or using efficient spectrometers that require less acquisition time.

System	screening bands	cell volume (a_0^3)
NaOCN	181	1198
KOCN	130	874
NaSCN	300	2090
KSCN	339	2407
CuSCN	75	476

TABLE I. The number of bands used to calculate the screening of the core-hole potential is given by screening bands. The according unit cell volumes are shown in Bohr radius a_0^3.

III. THEORETICAL MODELING

The OCEAN code was used for theoretical calculations throughout this work [6, 13]. OCEAN is a first-principles code for calculating core-level spectroscopy, including XAS and RIXS, using the Bethe-Salpeter equation (BSE) approach. We start with a ground-state calculation using density-functional theory (DFT) [30]. QUANTUM ESPRESSO is used for the DFT calculations [31, 32]. The BSE effective Hamiltonian describes interactions between the excited photo-electron and the hole it left behind, using the occupied and unoccupied states from the initial DFT calculation as a basis. The strong excitonic attraction between electron and hole is screened by the rest of the electrons in the system. The OCEAN input includes parameters like the atomic structure, photon excitation information, pseudopotentials for the DFT calculation, and specific convergence thresholds for the calculations. The pseudopotentials are taken from the PseudoDojo collection [33] and generated using the ONCVPSP code [34].

One advantage of OCEAN is that a material can be simulated across different absorption edges and different techniques (e.g., XAS, XES, RIXS) using a consistent set of input parameters, thus simplifying comparisons between theory and experiment. Details on the calculations are as follows. Within the DFT calculation the quantum mechanical state of a many-electron system is calculated based on the local electron density. A fictional non-interacting system of fermions with an appropriate density-dependent potential is assumed. A common approximation is to neglect the electrons that are not participating in the chemical bonds, and thus in the calculation of molecule orbitals by dividing the electrons into core and valence electrons. The $-Z/r$ ionic potentials are replaced by pseudopotentials that reproduce the correct valence electron behavior without explicit core-level electrons. The choice of the specific pseudopotential is crucial for a successful calculation. In this work norm-conserving pseudopotentials were used to employ the local-density approximation to the exchange-correlation functional. The structural input parameters [35] have been taken from the Materials Project database [36], with the exception of KOCN which was taken from experimental data [37].

The convergence parameters [35] that have been chosen for the calculations are summarized in the following. The plane-wave cutoff is used for the DFT calculation to truncate the basis and has been chosen for all compounds to be 150 Rydberg. The **k**-mesh is the grid of crystal momentum points used for the calculation of the wavefunctions for the BSE and is chosen to be sufficiently high ($k = \{8\times8\times8\}$) for the calculated spectra while avoiding excessive computational costs. The number of conduction bands included corresponds to the number of wave functions included up to some energy above the Fermi level in the Green's function and has been set to 150 for all compounds. The number of bands used to calculate the screening core-hole potential is given by the screening bands number given in Table I. For solving the BSE, the electron orbitals were down sampled onto a real-space mesh with a linear density exceeding 0.3 points per a.u.

IV. RESULTS AND DISCUSSION

We show the experimental and calculated results of the cyanates and the thiocyanates at the N K edge. Sec. IV A includes results of both the cyanates and thiocyanates whereas Sec. IV B shows the RIXS results of the thiocyanates. All spectra are normalized by the incoming photon flux and actual measurement time.

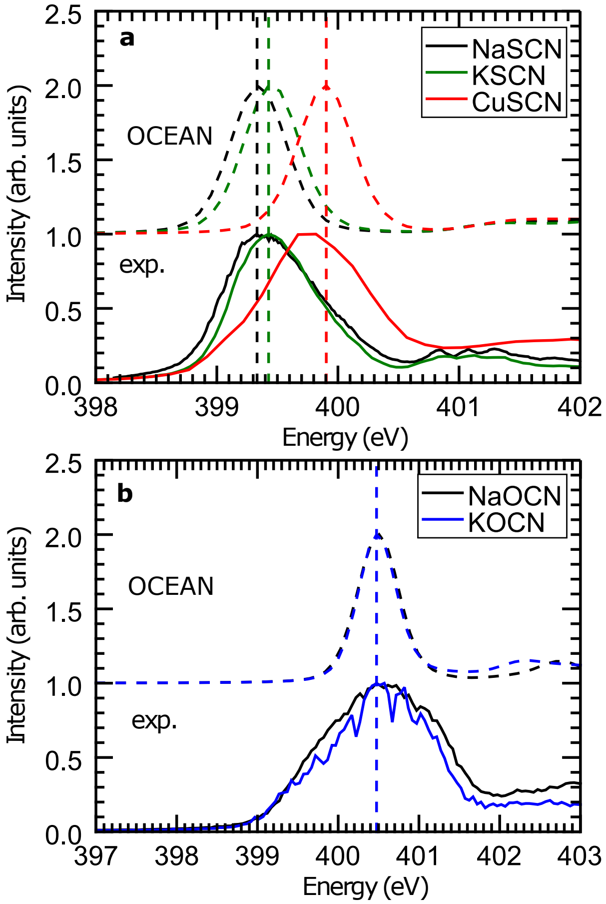

FIG. 2. Comparison of measured XAS spectra of thiocyanates (a) and cyanates (b) at the N K edge with calculated OCEAN data. For the sake of clarity, all spectra have been normalized to their respective maximum intensity and offset vertically.

A. Results of XAS measurements

Figure 2 shows a comparison of measured XAS spectra (solid lines) of the thiocyanates and cyanates at the N K edge with OCEAN calculations (dashed lines). The experimental data and the calculations are in good agreement with respect to exciton peak positions, energy shifts, and peak forms.

The plots have been normalized to maximum intensity and the OCEAN results have been offset vertically for comparability. OCEAN does not calculate the absolute energy scale for X-ray excitations, but it does account for relative shifts between different chemical environments [2]. A single offset was determined by aligning the calculated and measured spectra for KSCN and was applied to all calculated spectra. We find good agreement between the experiment and calculated data for the peak positions associated with chemical shifts due to differing chemical bonds for all five compounds. Table II summarizes the relative positions between the compounds and the position of KSCN. The given uncertainties are those from the fit of the features, which was conducted with an assump-

System	Shift (Exp.)	Shift (Theo.)	Exp.- Theo.
NaOCN	1.10 (7)	1.04	0.06
KOCN	1.10 (3)	1.04	0.06
NaSCN	−0.10 (3)	-0.11	0.01
CuSCN	0.31 (8)	0.44	−0.13

TABLE II. Summarized relative peak positions for four different compounds for the experimental data and calculated data as well as the difference between experimental and calculated shifts. Shifts in both the experimental data as well as for the theoretical calculation are determined relative to the KSCN peak position.

tion of a Voigt profile for the exciton peaks and a step function for the edge [35]. The broadening of features in a spectrum can be associated with a broadening due to core-hole lifetime, the resolution of the instrumentation, and vibrational disorder. The core-hole lifetime of nitrogen just above the K edge is under 0.1 eV and is included in the calculated spectra as a Lorentzian broadening. The resolution of the monochromator was applied to all calculated spectra as a Gaussian broadening. The resolution of the PGM beamline depends on the operation parameters of the beamline [19] (monochromator C_{ff} parameter and exit slit width) as well as the respective energy. For the presented measurements in the energy range around 400 eV the resolution is estimated to be around 0.22 eV.

The observed differences in the peak position of the main exciton, i.e. chemical shifts, are the result of several competing factors including the energy required to remove the nitrogen 1s electron, the energy required to insert a conduction electron, and the excitonic binding of the electron–core-hole pair. Within OCEAN, relative changes in the core removal energy are determined by changes in the total Kohn-Sham potential experienced by the core electron and the adiabatic response of the valence electrons to the creation of a core hole, i.e., the dielectric screening. The conduction band energies are taken directly from the DFT calculation, and the excitonic binding from the BSE [46]. In the case of the five cyanates and thiocyanates investigated here, no single factor is responsible for the relative shifts. Changes to the cation simultaneously change the volume per formula unit as well as the ground-state electron density. An increase in the electronic density near the core will red shift the XAS, while a decrease in the volume will tend to increase the conduction band energies, blue shifting the spectrum.

In Figure 2(a) we show that the experimental spectra of NaSCN and KSCN differ in a chemical shift of the N 1s level by about 0.1 eV, which is represented correctly in the OCEAN calculation. The measured copper thiocyanate exciton peak position is higher than the NaSCN by 0.31 eV, while the calculated position is higher by around 0.44 eV. CuSCN has the worst agreement between calculated and measured shifts for the N K-edge exciton with a discrepancy of 0.13 eV (Table II). This may be related to shortcomings in the DFT treatment of localized orbitals like the Cu 3d bands, which will be discussed later in Sec IV B. Nevertheless, this disagreement is only of the same order of magnitude as the estimated beamline energy resolution of $\Delta E = 0.22$ eV ($E/\Delta E = 1800$) [24].

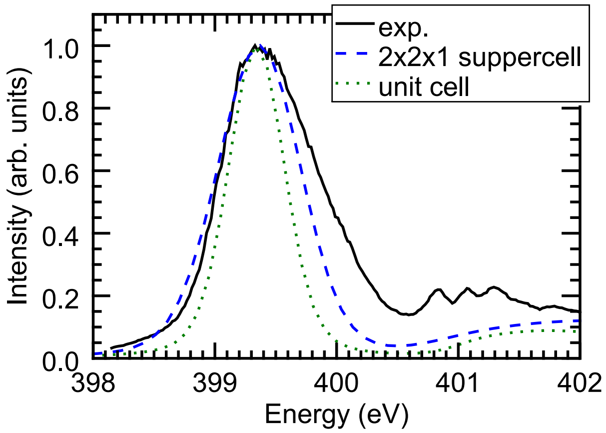

FIG. 3. Comparison of measured XAS spectra (black solid) of NaSCN at the N K edge with calculated OCEAN spectra carried out on a unit cell (green dotted) as well as a super cell (blue dashed). For the sake of clarity, all spectra have been normalized to the maximum intensity which has been set to 1.

Figure 2(b), which shows the comparison of the measured and calculated N K edge XAS of the cyanates, is also in agreement regarding the peak positions. During the measurement a significant effect of radiation damage was observed, which Section II B addresses in more detail. The cyanates, are highly sensitive to x-ray exposure. To reduce the impact of radiation damage on the experimental results the incoming photon flux was reduced (to around 8% compared to Figure 1(a)) and the spectra in Figure 2(b) were taken on a fresh spot of the sample for each energy in the NEXAFS (20 s each spectrum). To take the spot-to-spot variations into account, the carbon K fluorescence at 405 eV incident energy was recorded for each spot and used to normalize the NEXAFS.

All measured XAS spectra are significantly broader than the calculated spectra. This discrepancy in the widths between the calculated and experimental spectra might be observable due to neglecting of vibrational disorder. The OCEAN calculations were conducted for fixed unit cells. In reality the ions are vibrating around the equilibrium position. Vibrational disorder can be incorporated as an ensemble of deviations from the regular supercell used in the calculation. These are generated by calculating the phonon modes of the system and creating snapshots of the band structure with a given probability distribution [2]. Figure 3 shows the comparison of experimental data to the OCEAN calculation on a unit cell and a calculation on a $2 \times 2 \times 1$ super cell (containing 64 atoms). The theoretical calculation details for this calculation are described in Reference [2]. The comparison shows that the broadening due to vibrational disorder is significant but does not change the general shape of the spectrum. Particularly, the experimental spectra are markedly asymmetric. In the calculations the harmonic phonon approximation was used to simulate the vibrational disorder, which is incapable of reproducing asymmetric effects. Additionally, the possible occurrence of vibronic coupling is not included in the OCEAN calculations. In particular, the vibrational modes of the system are treated as having vanishing small energies as compared to the electronic excitations [38].

B. Results of RIXS measurements

In Figure 5 the RIXS measurements of NaSCN and CuSCN are shown. The results of RIXS measurements of KSCN are almost identical with the RIXS measurements of NaSCN and thus are not explicitly included in the following discussion, as was seen for the XAS measurements. The cyanates are not stable during the exposure time required for a RIXS spectrum, and thus do not provide valuable information for a comparison with theoretical RIXS data. The RIXS measurements consist of a series of emission spectra at selected incident energies around the absorption edge. The emission intensity is presented as the detected events on the CCD normalized to the maximum intensity for the sake of clarity.

The RIXS map can be separated into two areas. First, the region below 395 eV emission energy is the fluorescence emission resulting from the creation of a core hole and is the main focus of our analysis. The second region above 395 eV emission energy shows both the expected elastic line, with emitted photon energies equal to the incident energy, as well as a quasi-elastic feature with up to a few eV of energy loss. This region will be discussed briefly at the end of this section.

The N K edge RIXS map of CuSCN in Figure 4(b) shows marked differences compared to the other thiocyanates. For example, the peak at around 390 eV emission energy does not occur in the CuSCN RIXS map. This is to be expected given the difference between Cu with its occupied *d* electrons and the alkali metals Na and K.

Figure 5 shows a comparison of the measured RIXS with theoretically calculated spectra based upon OCEAN calculations for NaSCN and CuSCN. Shown are individual vertically offset measured and calculated emission spectra at different incident energies. The measured spectra (solid black lines) are scaled to the maximum intensity recorded. The OCEAN calculated (dashed red lines) spectra are a result of a sum of all polarization directions of the incoming and outgoing photons due to the fact that the samples are not in an oriented crystal structure, thus no polarization direction is preferred. In addition, they are scaled to the maximum intensity for the sake of comparison. Since OCEAN does not calculate an absolute energy scale the spectra are compared as functions of the energy loss $\Delta\omega$ which is defined as the difference between the incident and emitted photon energies. The energy alignment with the experimental data was done by comparing the maxima of the feature at around -5 eV of one X-ray emission spectrum an applied as an offset to all other spectra. A broadening was applied to the OCEAN calculations to better match the resolution in the experimental data. The experimental resolution depends on the pixel size of the CCD camera and the resolving power of the grating. In addition, the energy resolution of the beamline influences the overall resolution to some extent due to the fact that RIXS measurements are sensitive to uncertainties in the incident channel. The overall resolving power of 0.25 eV of the spectrometer was determined using the measured elastic scattering and applied to the OCEAN calculated data.

The general observation is that the main features in NaSCN match in their spacing between the experimental and the calculated data, whereas, the CuSCN results show larger deviations. The high-energy peak at around -5.5 eV for the NaSCN shows a good agreement with the OCEAN calculation. The same can be observed for the low-energy shoulder at around -10.5 eV and -11.5 eV, respectively. For NaSCN the feature at -7.5 eV, which is dominant in the experiment, is suppressed in the OCEAN calculation. This feature also has larger changes in intensity in the OCEAN calculation than in the experiment.

To understand the electronic structure provided by the analysis, the projected density of states (PDOS) in Fig. 6 is included in the analysis. The calculated PDOS shows how the 2p orbitals of each atom are distributed, and, in the case of the CuSCN, how the orbitals of the thiocyanate anion are strongly modified by the influence of the Cu 3*d* contribution from what is expected for a free ion. The PDOS of the contributing atoms are presented together with the experimental and the calculated X-ray emission spectra at 399.6 eV and 399.8 eV incident energy for NaSCN and CuSCN, respectively.

In the linear thiocyanate anion there is strong hybridization between the occupied orbitals of the S, C, and N, while the alkali cation contributes an electron via ionic bonding. From the calculated PDOS in Fig. 6(a), the nitrogen 2*p* contributes to three regions. Below -11 eV the contribution comes primarily from the S 2*p* with weak C and N mixing. The features between -10 eV to -9 eV originate primarily from C and N, whereas the region from -7 eV to -5 eV is again dominated by contributions from S with strong N mixing. For these features the positions and weights of the calculated XES (grey) agree well with the measured XES (orange). However, the feature in Fig. 5 (a) at an energy loss of -7.5 eV is clearly much stronger in the measured XES than in the calculated XES. Further, there is no corresponding feature in the PDOS. The intensity of this features changes in the same manner in the experimental as well as in the calculated XES. This indicates that this feature is potentially due to strong conduction-electron–valence-hole interactions which are only partially captured by the OCEAN cal-

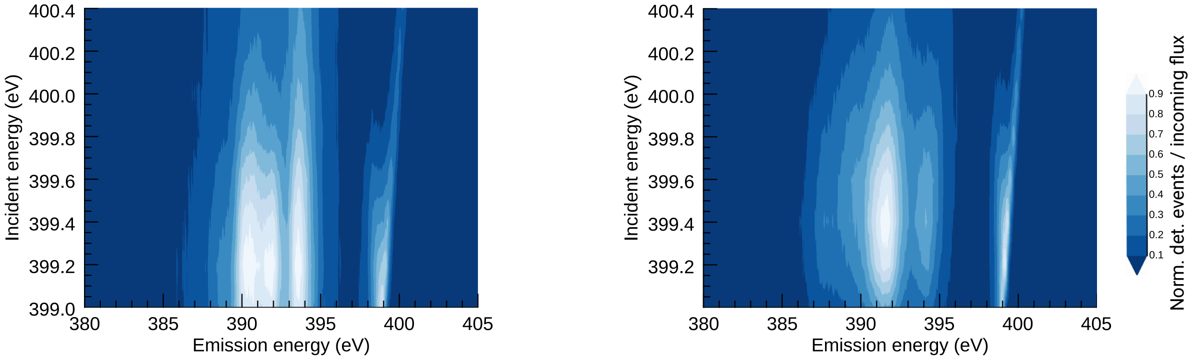

(a) NaSCN (b) CuSCN

FIG. 4. RIXS measurements of NaSCN (a) and CuSCN (b) above the N K edge.

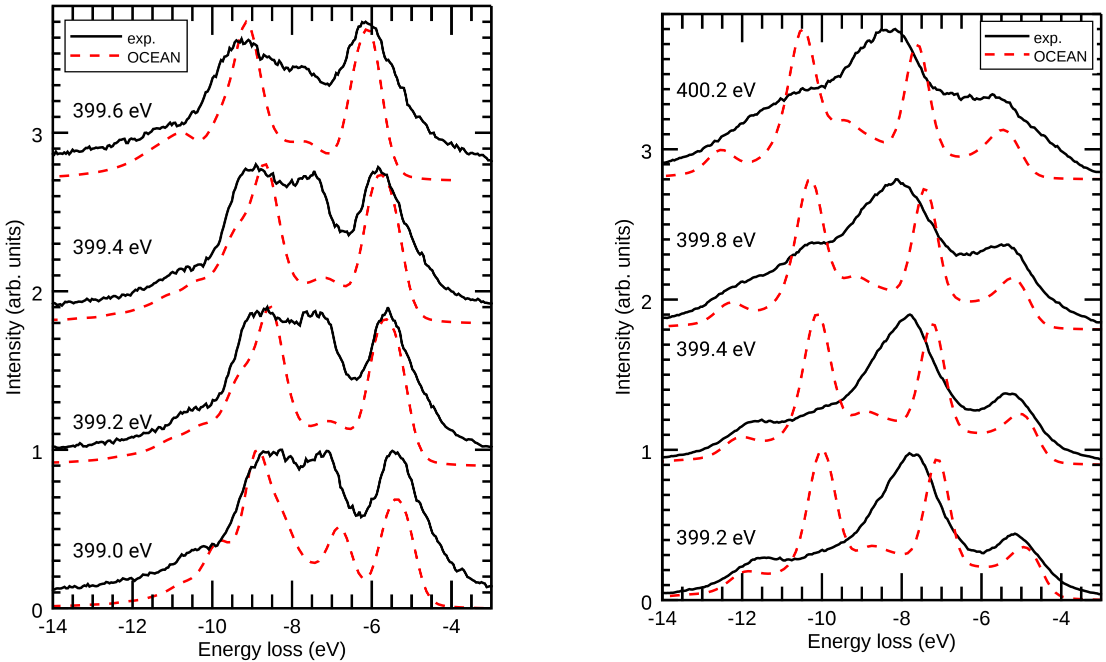

(a) NaSCN (b) CuSCN

FIG. 5. Energy loss spectra at different incident energies for (a) NaSCN and (b) CuSCN comparing experimental data (solid line) with OCEAN calculated RIXS spectra (red dashed line). Emission spectra at different incident energies are offset vertically for the sake of clarity and labeled on the left-hand side by the initial incident energy.

culations. This alone does not explain the large difference in the intensity of the feature related to the other features in the XES. A comparison with XES measurements of N_2 on a Ni-wafer from Pettersson *et al.* [45] shows a peak at -7.5 eV corresponding to the N-N bond. This is in agreement with Figure 2 (a) which indicates some N_2 gas build up at around 400.75 eV incident energy.

Fig. 5 (b) shows the comparison of measured and calculated RIXS spectra of CuSCN. The most intense peak at around -10.5 eV in the CuSCN OCEAN calculation seems to be suppressed in the experimental data. However, the peak positions as shown in Figure 7 for the experimental and calculated data seem to match very well. This is summarized in Table III, where the peak positions were extracted by performing a fit of the measured data with Voigt functions [35]. It appears that the discrepancy in peak positions is less than 0.3 eV. Cu $3d$ orbitals may not be correctly treated by the DFT since there remains a difference in peak intensities. The incorrect relative energy of DFT calculations of filled d-bands has been noted previously [39, 40]. It is clear in comparing the PDOS between NaSCN and CuSCN (Fig. 6) that the Cu $3d$ state hybridizes with the SCN^-, shifting peak positions and intensities and splitting the occupied states into additional groups. Changes to the energy of the Cu $3d$ and especially to their spatial extent will correspondingly change the N $2p$ orbitals and the relative peak strengths in the XES. In addition, we observe that the PDOS for NaSCN

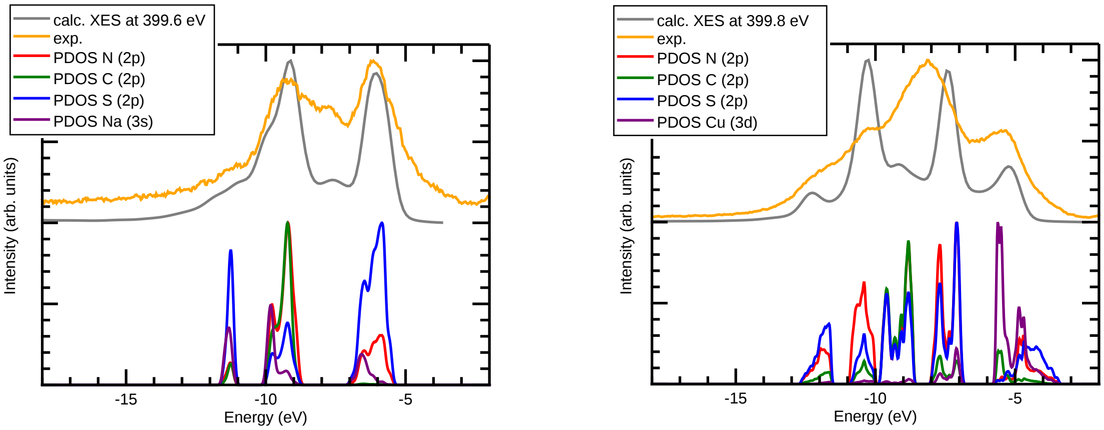

(a) PDOS NaSCN

(b) PDOS CuSCN

FIG. 6. Projected density of states for NaSCN and CuSCN compared to the according OCEAN calculated XES (grey) and experimental data (orange).

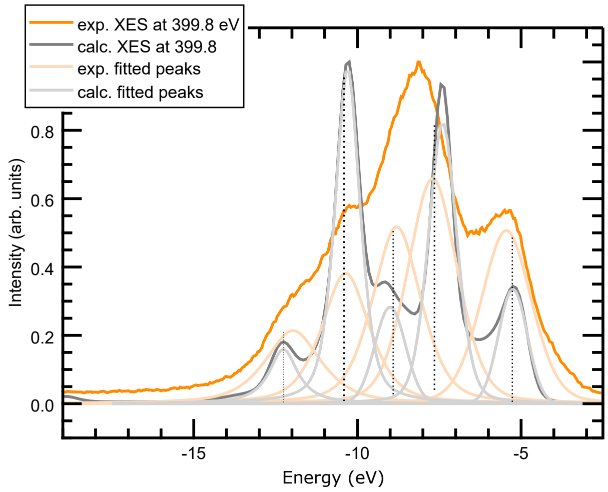

FIG. 7. Comparison of the fitted peaks for a measured (grey) and a calculated (orange) XES spectrum at an incident energy of 399.8 eV.

	OCEAN E pos. (eV)	Exp. E pos. (eV)	ΔE (eV)
A	-12.26	-11.97	-0.29
B	-10.30	-10.36	0.06
C	-9.0	-8.8	-0.2
D	-7.4	-7.7	0.3
E	-5.25	-5.45	0.2

TABLE III. Comparison of peak energy positions as shown in Fig. 5 between OCEAN calculated and experimental data for CuSCN at 399.79 eV as well as the difference between them.

and CuSCN show a similar behavior around -9 eV to -10 eV, both showing a hybridized orbital shared along the SCN^{-} ion. The main difference in the calculated RIXS spectra between NaSCN and CuSCN is that the contributions from this orbital are greatly reduced in the copper compound calculation, likely due to the influence of the copper $3d$ electrons.

Generally, the features in the experiment are broader than the calculated spectra despite the applied broadening from the response function. The OCEAN calculations were carried out on ordered unit cells. Calculating a disordered system might provide generally broader spectra (as seen in Fig. 3 for XAS) with slightly different feature ratios and suppressing of features like the one around -10.5 eV in the CuSCN. However, disordered RIXS calculations have not been carried out here due to the increased computational expense. Dramatic changes in the RIXS spectra due to vibrational broadening have been observed in systems with very light nuclei [18], but are not expected here, as Fig. 3 suggests for the absorption spectra.

The second region of the RIXS maps, above an emission energy of 395 eV comprises a feature corresponding with the quasi-elastic scattering. It is common to all five compounds. This is the inelastic feature near the elastic scattering that can be observed for example in the NaSCN spectra at an emission energy of around 399.2 eV. The feature is resolved and is distinguished from the elastic peak of the excitation radiation. The emission energy of the feature changes and an energy loss can be observed. It is likely that these features are due to strong coupling to phonon excitations, which can be observed in RIXS [41–43]. Such excitations are currently explicitly neglected in the computational approach we use here, and calculations of the influence of vibronic coupling on x-ray absorption and emission have been generally limited to molecular or localized systems.

V. CONCLUSION

Using theoretical modeling with the OCEAN code and XAS as well as RIXS measurements we were able to provide an analysis of the electronic structure of selected cyanates and thiocyanates. We were able to theoretically and experimentally observe the effects of interchanging atoms within a class of inorganic salts built by cyanate and thiocyanate anions and metallic cations despite the strong effect of radiation damage in the cyanates. The same set of input parameters and energy offset was used to calculate all five compounds for the N-K edge in X-ray absorption and RIXS [35]. The results show discrepancies compared to the experimental data which could be limitations of the DFT treatment of the Cu $3d$ orbitals as well as the treatment of mixed covalent and ionic bonds. By comparing RIXS calculations with OCEAN and PDOS calculations with QUANTUM ESPRESSO we observed an overestimation of the Cu-N bond and the according XES peak intensity. However, we were able to provide results with very good agreement in the peak positions when comparing calculated and measured RIXS data as well as a very good agreement in the XAS comparison.

With this work we continued the systematic investigation of the electronic structure of different crystals [1, 2] and showed the applicability of the OCEAN code to mixed covalent and ionic bonds. We have shown that using the Bethe-Salpeter equation approach and incorporating disorder decreases discrepancies between experimental data and OCEAN calculations. This is in agreement with findings of Vinson *et al.* [17].

The measured RIXS spectra in Fig. 4 clearly show the importance of vibronic coupling which is responsible for the low-loss features near the elastic line. Dynamic vibronic coupling to both the intermediate core-hole excited state and the final valence-hole state would likely influence the calculated XES, but such effects are not included in the current computational approach. One option for future work is to perform calculations of the ground state potential energy surfaces and the Franck-Condon amplitude for the vibronic coupling as it has been proposed by Weinhardt *et al.* [43, 44]. We conclude that, when dealing with light compounds, computational models that include vibronic effects are crucial for reproducing X-ray spectra and a reliable investigation of the electronic structure.

ACKNOWLEDGMENTS

Part of this research was performed within the EMPIR project AEROMET II. This project has received funding from the EMPIR Programme co-financed by the Participating States and from the European Union's Horizon 2020 Research and Innovation Program. Certain commercial materials are identified in this paper in order to specify the experimental procedure adequately. Such identification is not intended to imply recommendation or endorsement by NIST, nor is it intended to imply that the materials or equipment identified are necessarily the best available for the purpose.

---

[1] J. Vinson, T. Jach, M. Müller, R. Unterumsberger, and B. Beckhoff, Resonant x-ray emission and valence-band lifetime broadening in LiNO3, Physical Review B **100** (2019).

[2] J. Vinson, T. Jach, M. Müller, R. Unterumsberger, and B. Beckhoff, Quasiparticle lifetime broadening in resonant x-ray scattering of NH 4 NO 3, Physical Review B **94**, 035163 (2016).

[3] C. Li, J. Zhou, J. Song, J. Xu, H. Zhang, X. Zhang, J. Guo, L. Zhu, D. Wei, G. Han, J. Min, Y. Zhang, Z. Xie, Y. Yi, H. Yan, F. Gao, F. Liu, and Y. Sun, Non-fullerene acceptors with branched side chains and improved molecular packing to exceed 18% efficiency in organic solar cells, Nature Energy 2021 6:6 **6**, 605 (2021).

[4] N. Grabicki, O. Dumele, H. Sai, N. E. Powers-Riggs, B. T. Phelan, M. H. Sangji, C. T. Chapman, J. V. Passarelli, A. J. Dannenhoffer, M. R. Wasielewski, and S. I. Stupp, Polymorphism and Optoelectronic Properties in Crystalline Supramolecular Polymers, Chemistry of Materials **33**, 706 (2021).

[5] T. Vitvarová, J. Svoboda, M. Hissler, and J. Vohlídal, Conjugated Metallo-Supramolecular Polymers Containing a Phosphole Unit, Organometallics **36**, 777 (2017).

[6] J. Vinson, J. J. Rehr, J. J. Kas, and E. L. Shirley, Bethe-Salpeter equation calculations of core excitation spectra., Phys. Rev. B 83, 115106 (2011).

[7] A. P. Sadovskii, L. N. Mazalov, T. I. Guzhavina, G. K. Parygina, and B. Y. Khel'mer, Electronic structure of the thiocyanate ion SCN- from X-ray spectra, Journal of Structural Chemistry **14**, 618 (1974).

[8] T. Schoenherr, The cyanate ion as bridging ligand: synthesis, spectroscopic characterization, and magnetic properties of (.mu.-cyanato)bis(pentaamminechromium(III)) chloride, Inorganic Chemistry **25**, 171 (1986).

[9] R. Unterumsberger, P. Hönicke, B. Pollakowski-Herrmann, M. Müller, and B. Beckhoff, Relative L3 transition probabilities of titanium compounds as a function of the oxidation state using high-resolution X-ray emission spectrometry, Spectrochimica Acta Part B: Atomic Spectroscopy **145**, 71 (2018).

[10] R. Unterumsberger, M. Müller, B. Beckhoff, P. Hönicke, B. Pollakowski, and S. Bjeoumikhova, Focusing of soft X-ray radiation and characterization of the beam profile enabling X-ray emission spectrometry at nanolayered specimens, Spectrochimica Acta Part B: Atomic Spectroscopy **78**, 37 (2012).

[11] B. Pollakowski and B. Beckhoff, Nondestructive Speciation Depth Profiling of Complex TiOx Nanolayer Structures by Grazing Incidence X-ray Fluorescence Analysis and Near Edge X-ray Absorption Fine Structure Spectroscopy, Analytical Chemistry **87**, 7705 (2015).

[12] P. Hoffmann, O. Baake, B. Beckhoff, W. Ensinger, N. Fainer, A. Klein, M. Kosinova, B. Pollakowski, V. Trunova, G. Ulm, and J. Weser, Chemical bonding in carbonitride nanolayers, Nuclear Instruments and Methods in Physics Research Section A: Accelerators, Spectrometers, Detectors and Associated Equipment **575**, 78

(2007).

[13] K. Gilmore, J. Vinson, E. L. Shirley, D. Prendergast, C. D. Pemmaraju, J. J. Kas, F. D. Vila, and J. J. Rehr, Efficient implementation of core-excitation Bethe-Salpeter equation calculation., Comp. Phys. Comm. 197, 109 (2015).

[14] L. Monico, M. Cotte, F. Vanmeert, L. Amidani, K. Janssens, G. Nuyts, J. Garrevoet, G. Falkenberg, P. Glatzel, A. Romani, and C. Miliani, Damages Induced by Synchrotron Radiation-Based X-ray Microanalysis in Chrome Yellow Paints and Related Cr-Compounds: Assessment, Quantification, and Mitigation Strategies, Analytical Chemistry **92**, 14164 (2020).

[15] M. Wansleben, J. Vinson, A. Wählisch, K. Bzheumikhova, P. Hönicke, B. Beckhoff, and Y. Kayser, Speciation of iron sulfide compounds by means of X-ray emission spectroscopy using a compact full-cylinder von Hamos spectrometer, J. Anal. At. Spectrom. **35**, 2679 (2020).

[16] M. Wansleben, J. Vinson, I. Holfelder, Y. Kayser, and B. Beckhoff, Valence-to-core X-ray emission spectroscopy of Ti, TiO, and TiO2 by means of a double full-cylinder crystal von Hamos spectrometer, X-Ray Spectrometry **48**, 102 (2019).

[17] J. Vinson, T. Jach, M. Müller, R. Unterumsberger, and B. Beckhoff, Resonant X-ray Emission of Hexagonal Boron Nitride, Physical Review B **96** (2017).

[18] J. Vinson, T. Jach, W. T. Elam, and J. D. Denlinger, Origins of extreme broadening mechanisms in near-edge x-ray spectra of nitrogen compounds, Phys. Rev. B **90**, 205207 (2014).

[19] F. Senf, U. Flechsig, F. Eggenstein, W. Gudat, R. Klein, H. Rabus, and G. Ulm, A plane-grating monochromator beamline for the PTB undulators at BESSY II, Journal of Synchrotron Radiation **5**, 780 (1998).

[20] M. Krumrey, M. Gerlach, F. Scholze, and G. Ulm, Calibration and characterization of semiconductor X-ray detectors with synchrotron radiation, Nuclear Instruments and Methods in Physics Research Section A: Accelerators, Spectrometers, Detectors and Associated Equipment **568**, 364 (2006).

[21] F. Scholze and M. Procop, Modelling the response function of energy dispersive X-ray spectrometers with silicon detectors, X-Ray Spectrometry **38**, 312 (2009).

[22] B. Beckhoff, Reference-free X-ray spectrometry based on metrology using synchrotron radiation, J. Anal. At. Spectrom. **23**, 845 (2008).

[23] J. Nordgren, G. Bray, S. Cramm, R. Nyholm, J. Rubensson, and N. Wassdahl, Soft x-ray emission spectroscopy using monochromatized synchrotron radiation (invited), Review of Scientific Instruments **60**, 1690 (1989).

[24] Müller M, *Hochauflösende Röntgenemissionsspektrometrie im Spektralbereich weicher Röntgenstrahlung*, Ph.D. thesis, Technische Universität Berlin, Berlin (2009).

[25] Rainer Unterumsberger, *Effiziente hochauflösende Röntgenemissionsspektrometrie mit Synchrotronstrahlung*, Ph.D. thesis, Technische Universität Berlin, Berlin (2015).

[26] R. N. S. Sodhi and C. E. Brion, Reference energies for inner shell electron energy-loss spectroscopy, Journal of Electron Spectroscopy and Related Phenomena **34**, 363 (1984).

[27] F. Meyer, L. Weinhardt, M. Blum, M. Bär, R. G. Wilks, W. Yang, C. Heske, and F. Reinert, Non-equivalent carbon atoms in the resonant inelastic soft X-ray scattering map of cysteine, The Journal of Chemical Physics **138**, 034306 (2013).

[28] L. Weinhardt, A. Benkert, F. Meyer, M. Blum, D. Hauschild, R. G. Wilks, M. Bär, W. Yang, M. Zharnikov, F. Reinert, and C. Heske, Local electronic structure of the peptide bond probed by resonant inelastic soft X-ray scattering, Physical Chemistry Chemical Physics **21**, 10.1039/C9CP02481F (2019).

[29] M. P. Seah, I. S. Gilmore, and S. J. Spencer, Background subtraction: II. General behaviour of REELS and the Tougaard universal cross section in the removal of backgrounds in AES and XPS, Surface Science **461**, 1 (2000).

[30] W. Kohn and L. J. Sham, Self-Consistent Equations Including Exchange and Correlation Effects, Physical Review **140**, A1133 (1965).

[31] P. Giannozzi, S. Baroni, N. Bonini, M. Calandra, R. Car, C. Cavazzoni, D. Ceresoli, G. L. Chiarotti, M. Cococcioni, I. Dabo, A. Dal Corso, S. de Gironcoli, S. Fabris, G. Fratesi, R. Gebauer, U. Gerstmann, C. Gougoussis, A. Kokalj, M. Lazzeri, L. Martin-Samos, N. Marzari, F. Mauri, R. Mazzarello, S. Paolini, A. Pasquarello, L. Paulatto, C. Sbraccia, S. Scandolo, G. Sclauzero, A. P. Seitsonen, A. Smogunov, P. Umari, and R. M. Wentzcovitch, QUANTUM ESPRESSO: a modular and open-source software project for quantum simulations of materials, Journal of Physics: Condensed Matter **21**, 395502 (2009).

[32] P. Giannozzi, O. Baseggio, P. Bonfà, D. Brunato, R. Car, I. Carnimeo, C. Cavazzoni, S. de Gironcoli, P. Delugas, F. Ferrari Ruffino, A. Ferretti, N. Marzari, I. Timrov, A. Urru, and S. Baroni, Quantum ESPRESSO toward the exascale, The Journal of Chemical Physics **152**, 154105 (2020).

[33] M. J. van Setten, M. Giantomassi, E. Bousquet, M. J. Verstraete, D. R. Hamann, X. Gonze, and G. M. Rignanese, The PseudoDojo: Training and grading a 85 element optimized norm-conserving pseudopotential table, Computer Physics Communications **226**, 39 (2018).

[34] D. R. Hamann, Optimized norm-conserving Vanderbilt pseudopotentials, Physical Review B **88**, 085117 (2013).

[35] See Supplemental Material at [URL will be inserted by publisher] for information on the spectrum fit, atomic parameters, and the OCEAN input.., .

[36] A. Jain, S. P. Ong, G. Hautier, W. Chen, W. D. Richards, S. Dacek, S. Cholia, D. Gunter, D. Skinner, G. Ceder, and K. A. Persson, Commentary: The Materials Project: A materials genome approach to accelerating materials innovation, APL Materials **1**, 10.1063/1.4812323 (2013).

[37] S. B. Hendricks and L. Pauling, The crystal structures of sodium and potassium trinitrides and potassium cyanate and the nature of the trinitride group, Journal of the American Chemical Society **47**, 2904 (1925).

[38] C. Brouder, D. Cabaret, A. Juhin, and P. Sainctavit, Effect of atomic vibrations on the x-ray absorption spectra at the ¡span class, Physical Review B **81**, 115125 (2010).

[39] V. P. Zhukov, F. Aryasetiawan, E. V. Chulkov, I. G. d. Gurtubay, and P. M. Echenique, Corrected local-density approximation band structures, linear-response dielectric functions, and quasiparticle lifetimes in noble metals, Physical Review B **64**, 195122 (2001).

[40] L. Weinhardt, O. Fuchs, E. Umbach, C. Heske, A. Fleszar, W. Hanke, and J. D. Denlinger, Resonant inelastic soft x-ray scattering, x-ray absorption spectroscopy, and density functional theory calculations of the electronic bulk band structure of CdS, Physical Review B **75**, 165207 (2007).

[41] F. Hennies, S. Polyutov, I. Minkov, A. Pietzsch, M. Nagasono, H. Ågren, L. Triguero, M.-N. Piancastelli, W. Wurth, F. Gel'mukhanov, and A. Föhlisch, Dynamic interpretation of resonant x-ray Raman scattering: Ethylene and benzene, Physical Review A **76**, 032505 (2007).

[42] F. Hennies, A. Pietzsch, M. Berglund, A. Föhlisch, T. Schmitt, V. Strocov, H. O. Karlsson, J. Andersson, and J.-E. Rubensson, Resonant Inelastic Scattering Spectra of Free Molecules with Vibrational Resolution, Physical Review Letters **104**, 193002 (2010).

[43] L. Weinhardt, M. Weigand, O. Fuchs, M. Bär, M. Blum, J. D. Denlinger, W. Yang, E. Umbach, and C. Heske, Nuclear dynamics in the core-excited state of aqueous ammonia probed by resonant inelastic soft x-ray scattering, Physical Review B **84**, 104202 (2011).

[44] L. Weinhardt, E. Ertan, M. Iannuzzi, M. Weigand, O. Fuchs, M. Bär, M. Blum, J. D. Denlinger, W. Yang, E. Umbach, M. Odelius, and C. Heske, Probing hydrogen bonding orbitals: resonant inelastic soft X-ray scattering of aqueous NH3, Phys. Chem. Chem. Phys. **17**, 27145 (2015).

[45] L. G. M. Pettersson and A. Nilsson, A molecular perspective on the d-band model: Synergy between experiment and theory, Topics in Catalysis **57**, 2 (2014).

[46] J. Vinson and E. L. Shirley, Fast, efficient, and accurate dielectric screening using a local real-space approach, Physical Review B **103**, 245143 (2021).